Journal of Alloys and Compounds 953 (2023) 170139

Contents lists available at ScienceDirect

Journal of Alloys and Compounds

journal homepage: www.elsevier.com/locate/jalcom

Magnetic carbon nanocomposites via the graphitization of glucose and their induction heating

Sašo Gyergyek [a,*], Elena Chernyshova [b], Katalin Bőőr [a,1], Marijan Nečemer [c], Darko Makovec [a]

[a] Department for Synthesis of Materials, Jožef Stefan Institute, Jamova 39, SI-1000 Ljubljana, Slovenia
[b] Department of Materials Chemistry, National Institute of Chemistry, Hajdrihova 19, SI-1000 Ljubljana, Slovenia
[c] Department for Low and Medium Energy Physics, Jožef Stefan Institute, Jamova 39, SI-1000 Ljubljana, Slovenia

ARTICLE INFO

Article history:
Received 19 July 2022
Received in revised form 6 April 2023
Accepted 13 April 2023
Available online 14 April 2023

Keywords:
Graphitization
Iron nanoparticles
Magnetic hyperthermia
Induction heating
Catalysts

ABSTRACT

Carbon nanocomposites containing iron-based nanoparticles are attractive materials for the catalyst supports used for magnetic (induction) heating catalysis. The metallic, soft-magnetic iron nanoparticles provide local heating of the support in an alternating magnetic field and ensure rapid magnetic separation of the nanocomposite particles from reaction suspensions. In this work, magnetic carbon nanocomposites were prepared by annealing the precursor particles consisting of iron-oxide nanoparticles dispersed in a carbohydrate matrix. The annealing was conducted at 600 °C and 750 °C in an Ar atmosphere. At both temperatures the carbothermal reduction of iron oxide to Fe/Fe_3C was observed; however, at the lower temperature the rate of reduction and the growth of the nanoparticles were considerably slower. The Fe_3C was formed in negligible amounts only after a prolonged period of annealing at 600 °C. A detailed structural analysis showed that the Fe/Fe_3C nanoparticles catalyze the graphitization of the carbonaceous precursor material already at 600 °C, resulting in the formation of a graphitic shell that surrounds them. This shell is tight enough to prevent the areal oxidation of the encapsulated Fe nanoparticles; their magnetic properties remained unchanged even after 1 year of storage under ambient conditions. At the higher annealing temperature, the growth of the Fe/Fe_3C nanoparticles caused bursting of the graphitic shell and thus partially exposed their surfaces to the atmosphere. All the nanocomposites exhibited ferromagnetic behavior in accordance with their compositions. The nanocomposite that was predominantly composed of a graphitic shell, encapsulated Fe nanoparticles and a negligible amount of Fe_3C, showed the highest specific absorption rate (760 W/g_{Fe} at 274 kHz), even at a relatively low AC-field amplitude (88 mT).

1. Introduction

The use of renewable or carbon-neutral electricity in the chemical industry will be one of the most important measures for reducing the carbon footprint of society. The direct conversion of renewable electricity, through electrocatalytic processes into chemicals such as fuels (H_2 and NH_3 for example), monomers, solvents, etc., is becoming an important strategy to achieve this goal [1]. However, the use of electricity to supply the heat for thermo-catalytic processes that are currently relying on fossil fuels is equally important. In general, microwave and so-called magnetic or induction heating are two of the most promising alternatives. Rapid and extensive heating of magnetic nanoparticles (MNPs) under the influence of an alternating magnetic field to drive chemical reactions has only recently been demonstrated [2–9]. Kirschning et al. showed that magnetic nanoparticles can heat sufficiently to drive technologically important chemical reactions in continuous operation and significantly improve the yield compared to conventional heating [3]. Ru-bearing iron carbide MNPs have been used to demonstrate magnetically induced batch CO and continuous CO_2 hydrogenation [5,8]. Recently, our group developed a method for the preparation of magnetically separable carbon with a high loading of magnetic nanoparticles, which was used to prepare highly active Ru-based nanocatalysts for the valorization of biomass [10–13]. The use of magnetic (induction) heating to deliver heat where needed is regarded as an enabling technology suited to push many catalytic reactions beyond the reactor's heat-transfer limits, to the limits of the process kinetics [7]. The advantages of the technology are the more favorable energy balance, process intensification, reactor-setup

* Corresponding author.
E-mail address: saso.gyergyek@ijs.si (S. Gyergyek).
[1] Present address: Department of Chemistry-Ångström Laboratory, University of Uppsala, Lägerhyddsvägen 1, 751 21 Uppsala, Sweden.

https://doi.org/10.1016/j.jallcom.2023.170139

simplification, reduced safety issues, minor operational costs, and increased process productivity [7].

Typical catalysts for the conversions of biomass into value-added chemicals are (precious) metal nanoparticles supported on a high-surface-area inert material such as carbon, TiO_2, ZrO_2 and Al_2O_3, to mention just a few [14]. Carbon as a support material for catalysts has long been relevant due to its commercial availability, thermochemical stability, low density and simple preparation from various natural sources, such as biomass, sugars and fatty acids [15–18]. However, for magnetic (induction) heating applications, the carbon material must contain magnetic nanoparticles. Due to their low price, ease of preparation and low toxicity, iron and iron oxide nanoparticles are very attractive. Iron nanoparticles are magnetically soft with a high saturation magnetization, which makes them more appealing than iron oxide nanoparticles. However, iron nanoparticles are prone to oxidation, if not suitably protected, making their handling and storing under oxidizing atmospheres practically impossible. Our research was inspired by findings related to the syntheses of carbon nanotubes and graphene surface layers. The established path to the controlled synthesis of carbon nanotubes (CNTs) is catalytic chemical vapor deposition. The observation of carbon nanotubes during their growth at near-ambient pressure using in-situ transmission electron microscopy and quantum mechanical calculations provided a clear picture of the process [19,20]. The main findings show that single-wall CNTs start their growth by forming a cap on the surface of the catalyst nanoparticle, while their growth proceeds with the addition of carbon atoms at the nanoparticle/nanotube interface [19,20]. Iron-based nanoparticles were the most studied catalysts and the results of several studies showed that only nanoparticles smaller than 3–4 nm can catalyze the growth of single-wall CNTs [19,21]. At the other end of the catalyst size spectrum, some recent research showed that a flat, metallic Ni surface under carefully controlled CVD conditions catalyses the formation of a graphene layer, which despite its single-layer thickness protects the Ni surface from areal oxidation [22]. This led us to believe that Fe nanoparticles that are significantly larger than 5 nm would not catalyze the formation of the CNTs due to their larger size, but that they would, under the conditions of an "unlimited" carbon supply (as opposed to CVD, where the carbon-precursor supply is carefully controlled and kept low), catalyze the formation of a graphitic shell. In this paper, based on recent mechanistic findings describing the formation of CNTs catalyzed by small Fe nanoparticles and the formation of a graphene single layer by a flat metallic surface, we developed a proof-of-concept to synthesise oxidation-resistant Fe nanoparticles using the carbothermal reduction of iron oxide nanoparticles embedded within biomass-derived carbonaceous precursors. The Fe and Fe_3C nanoparticles, in the size range 15–50 nm, catalyze the graphitization, resulting in their encapsulation with a thin, graphitic shell. The close control of the phase composition enabled the preparation of a nanocomposite showing an exceptionally high specific absorption rate, the figure of merit for the heat the material generates in an AC-field, and having excellent oxidation stability.

2. Experimental

2.1. Materials

Iron (III) sulfate hydrate ($Fe_2(SO_4)_3 \cdot xH_2O$, Sigma-Aldrich), iron (II) sulfate hydrate ($FeSO_4 \cdot 7\ H_2O$ 92%, Alfa-Aesar), ammonium hydroxide (NH_4OH 25% solution, J.T. Baker), citric acid monohydrate (ACS 99–102%, Alfa-Aesar), acetone (reagent grade, Carlo-Erba), glucose (D-glucose 99%, Alfa-Aesar), and 2-propanol (ACS reagent grade, VWR) were used in the as-received condition.

2.2. Synthesis

Citric-acid-coated magnetic iron oxide nanoparticles (MNs) were synthesized using a previously published method with simple co-precipitation, followed by the adsorption of the citrate ions in an aqueous solution [23]. The MNs were dispersed in DDI water, to which glucose was added. The final concentration was 9 g/L of MNs and 90 g/L of glucose. A concentrated solution of NaOH was used to adjust the pH to a value of ~10. A total of 800 mL of the suspension was transferred to a 1-litre stainless-steel Parr autoclave equipped with a stirrer. The suspension was treated at 180 °C for 12 h. The brown flock (MN-C) was magnetically separated, washed several times with DDI water and dried at 80 °C in an oven. The dried powders were annealed in a tubular furnace at 600 °C or 750 °C for 1 h, 2 h or 6 h in an atmosphere of Ar. Samples are denoted as MN-C-T-t, where T means the temperature of annealing and t means the time of annealing. The black powders (MN-C-T-t) were grinded as a 2-propanol slurry in an agate mortar, dried under vacuum and stored in desiccator.

2.3. Characterization

X-ray powder-diffraction (XRD) patterns were collected using a Siemens D5005 diffractometer with a monochromator in the diffracted beam. Quantitative phase analyses based on a Rietveld refinement of the XRD patterns was made using DIFFRACplus Topas® software. Jeol JEM2100 and Jeol JEM2010F transmission electron microscopes (TEM) operated at 200 kV and a Cs-corrected Jeol ARM 200CF STEM scanning transmission electron microscope (STEM) operated at 80 kV were used to observe the samples deposited on a copper-grid-supported lacy carbon foil (See SI for details). The Raman spectra of the samples were recorded with a NT-MDT model Integra Spectra for Materials Science equipped with a confocal microscope (20 × magnification) at room temperature using a 633-nm laser diode for the excitation (See SI for details). Nitrogen adsorption/desorption isotherms were measured for the samples at liquid-nitrogen temperature using a Nova 2000e (Quantachrome) nitrogen-sorption analyser. Prior to the measurements the samples were degassed over night at 120 °C in a vacuum. The surface area was calculated using the Brunauer–Emmett–Teller (BET) equation with nitrogen-adsorption data in the P/P_0 range between 0.05 and 0.3 (7-point analysis), and the pore volume was extracted from the desorption branch of the isotherm using the Barrett–Joyner–Halenda (BJH) method. Room-temperature magnetization curves of the samples were measured with a vibrating-sample magnetometer (VSM) LakeShore 7307 VSM. The Fe content in the MN-C-T-t samples was non-destructively determined by using an energy-dispersive X-ray fluorescence spectrometer (EDXRF) and utilizing our in-house-developed QAES (Quantitative Analysis of Environmental Samples) software [24,25] (See SI for details). The specific absorption rate (*SAR*) of the MN-C-T-t was determined from measurements of the temperature increase in an AC-field using an Ambrell (USA) HTG-6000 (6 kW) high-frequency generator coupled to a copper-tube coil (Induktio d.o.o., Slovenia).

3. Results and discussion

3.1. Results

The magnetic carbon nanocomposites MN-C-T-t were prepared by annealing the precursor MN-C in an inert atmosphere. The MN-C contains homogeneously dispersed magnetic iron oxide nanoparticles (~8 nm in size) in an amorphous carbonaceous matrix (Table 1) [10]. Annealing of the MN-C at 600 °C and 750 °C changed the phase composition of the MN-C-T-t (Fig. 1).

Table 1
Estimated crystallite size, room-temperature magnetic properties and specific surface area of the magnetic nanoparticles MN, precursor MN-C and nanocomposites. S is spinel iron oxide, F is BCC Fe, C is Fe_3C and G is graphite.

Sample	d_{XRD}/nm				Magnetic properties				Surface area	
	S	F	C	G	M_s (Am^2/kg) [a]	M_s (Am^2/kg) [b]	M_r (Am^2/kg)	H_c (mT)	S_{BET} (m^2/g)	V_p (cm^3/g)
MN	8	/	/	/	61	/	/	/	/	/
MN-C	8	/	/	/	9.4	/	/	/	8.1	0.0799
MN-C-600–1	10	16	/	/	13.1	62.1	1.0	3.8	311	0.302
MN-C-600–2	11	17	/	/	14.2	84.2	1.4	4.9	309	0.269
MN-C-600–6	14	54	30[c]	5.2	31.9	142.6	8.1	4.10	258	0.379
MN-C-750–1	15	37	40.5	4.6	29.8	129.2	5.8	34.1	241	0.369
MN-C-750–2	16	43	47.8	4.7	31.0	131.8	6.0	35.1	240	0.361
MN-C-750–6	20	49	45.2	4.6	39.7	133.7	5.4	21.5	227	0.331

[a] Magnetization normalized per mass of sample.
[b] Magnetization normalized per amount of iron.
[c] Very low weight fraction, estimation unreliable.

A quantitative phase analysis based on a Rietveld refinement of the XRD patterns showed that the cubic spinel iron oxide nanoparticles were reduced to BCC Fe and orthorhombic Fe_3C (Fig. 2). At 600 °C the kinetics seems to be sluggish, as only a small amount (roughly 15 wt%) of the iron oxide nanoparticles reduced to Fe nanoparticles within the first 2 h of annealing (Fig. 2). Within 6 h, most of the iron oxide was reduced to Fe and a relatively small amount of Fe_3C (Fig. 2). While the size of the iron oxide nanoparticles remained almost unchanged during the whole 6 h, the Fe nanoparticles grew from 17 nm to 54 nm during the last 4 h of the annealing at 600 °C (Table 1). Nanocrystalline graphite was detected by XRD only in the sample MN-C-600–6, coexisting with the Fe_3C (Figs. 1 and 2). At 750 °C most of the iron oxide nanoparticles were reduced already within the first hour of annealing (Figs. 1 and 2). After 2 h of annealing, the Fe_3C is the most abundant iron-containing phase, while after 6 h the Fe becomes dominant and the cubic spinel iron-oxide fraction seems to increase slightly (Figs. 1 and 2). A large amount of nanocrystalline graphite was already formed within the first hour of annealing and neither its crystal size nor its fraction changed significantly afterwards.

The TEM analysis showed that the MN-C-T-t samples are in the form of irregularly shaped agglomerates composed of homogeneously dispersed nanoparticles that appear dark in the BF images within the brighter matrix of carbon (Fig. 3). EDXS and SAED were used to match the iron-based nanoparticles with the phases indicated by the XRD.

In the samples MN-C-600–1 and MN-C-600–2, only spherical iron-oxide nanoparticles, ~10 nm in size, are visible, corroborated by the XRD, while the carbon matrix is relatively thick, well rounded and of uniform contrast, indicating its amorphous nature (Fig. 3(a) and (c)). In the sample MN-C-600–6 the contrast of the carbon matrix is non-uniform (insets in Fig. 3(e)) and besides the brighter iron oxide nanoparticles (Fig. S1), larger (between 20 nm and 100 nm in diameter) and darker nanoparticles are clearly visible (Fig. 3(e)). Selected-area electron diffraction patterns of those larger and darker nanoparticles showed that they are either BCC Fe (which is the dominant Fe-containing crystalline phase by wt% in the sample according to the Rietveld analysis) or orthorhombic Fe_3C (Fig. 4 and S2). Using the EDXS analysis, the iron oxide nanoparticles can be clearly differentiated from the Fe and Fe_3C nanoparticles (C is present in all the samples and the presence of the C K peak in the EDXS spectrum is not indicative of the Fe_3C). To differentiate between the Fe and Fe_3C nanoparticles a SAED pattern was used. In the following discussion, when referring to the nanoparticles as Fe or Fe_3C nanoparticles, such a specific distinction was experimentally made using the SAED pattern. When referring to the nanoparticles as Fe/Fe_3C nanoparticles, such a distinction was not made, and the nanoparticles are either BCC Fe or orthorhombic Fe_3C. The HRTEM image of the interface between the Fe nanoparticle and the carbon matrix clearly shows that a graphite shell crystallized on the nanoparticle surfaces (lower inset in Fig. 4). The periodicity of the lattice image of

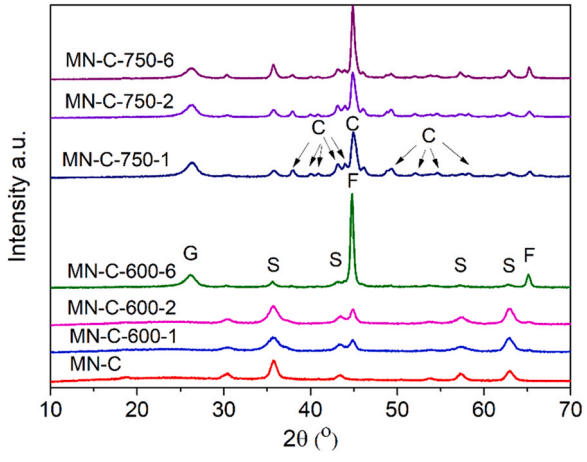

Fig. 1. XRD powder patterns of the precursor MN-C and the annealed nanocomposite samples. S corresponds to reflections of cubic spinel (iron oxide) (space group Fd-3 m), C to reflections of orthorhombic Fe_3C (space group Pnma), F to reflections of BCC iron (space group Im-3 m) and G to reflections of graphite (space group P63mc).

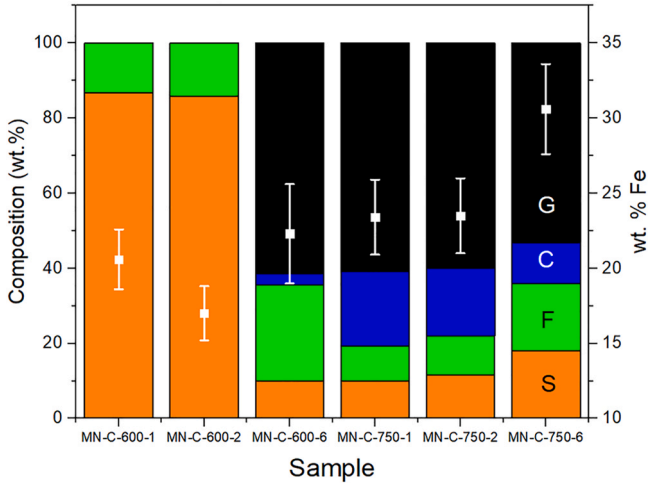

Fig. 2. Estimated weight fractions of crystalline phases determined by XRD (stacked columns) and amount of Fe (red squares with error bars) in the carbonized samples. S corresponds to cubic spinel (iron oxide), C to orthorhombic cohenite Fe_3C, F to BCC iron and G to graphite.

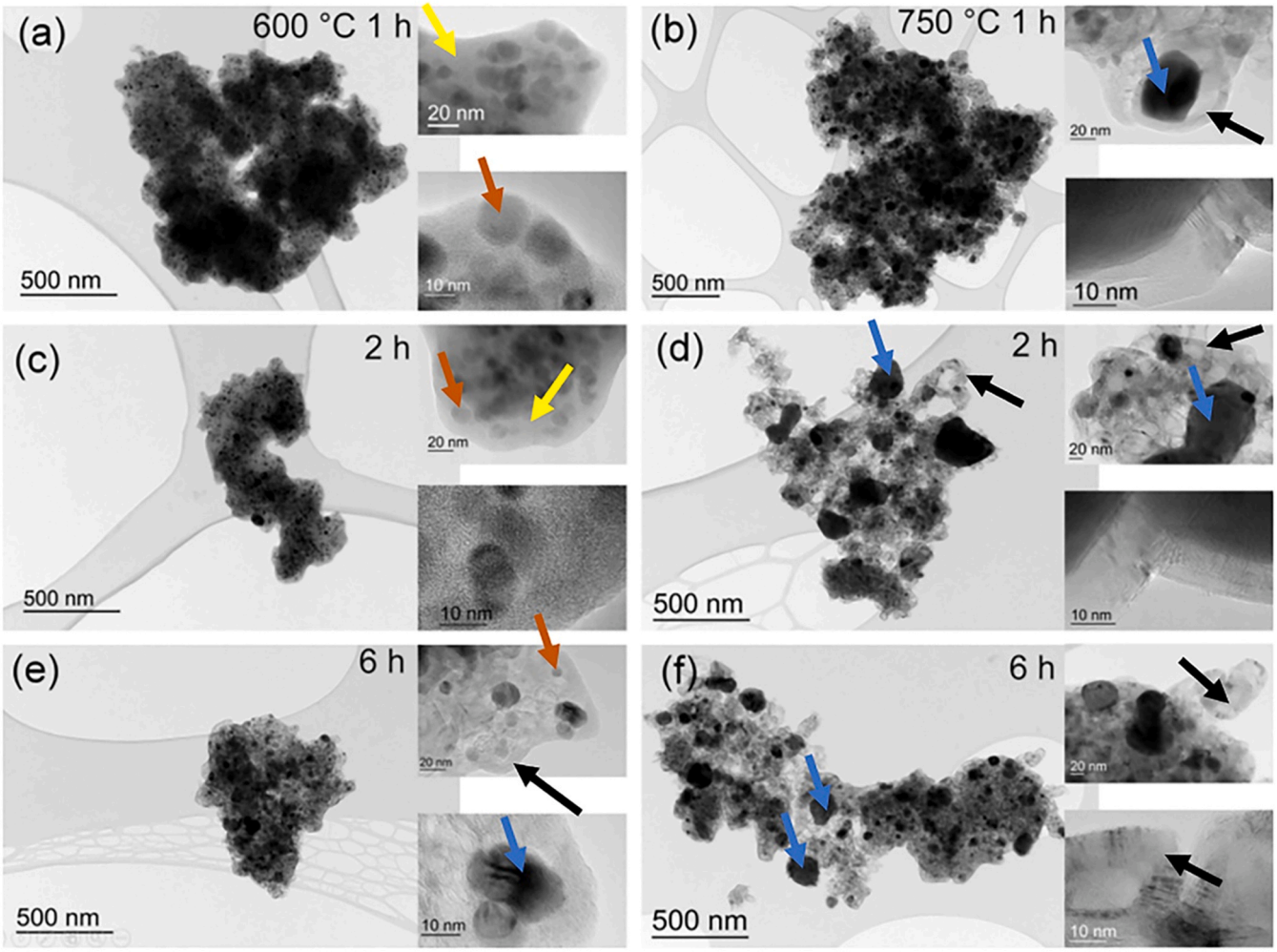

Fig. 3. TEM images of nanocomposites MN-C-600–1 (a), MN-C-600–2 (c), MN-C-600–6 (e), MN-C-750–1 (b), MN-C-750–2 (d) and MN-C-750–6 (f). Amorphous carbon marked with yellow arrows, graphitic carbon with black, iron-oxide nanoparticles with brown and Fe/Fe_3C nanoparticles with blue. Insets are TEM images acquired at higher magnifications.

graphite (3.70 Å) is larger than the interlayer spacing in crystalline graphite (3.35 Å) with a Bernal structure, indicating so-called turbostratic stacking, i.e., rotationally random stacking [26,27]. HRTEM imaging of the upper part of the Fe nanoparticle (upper inset in Fig. 4) shows that a thin layer of the cubic spinel iron oxide grew

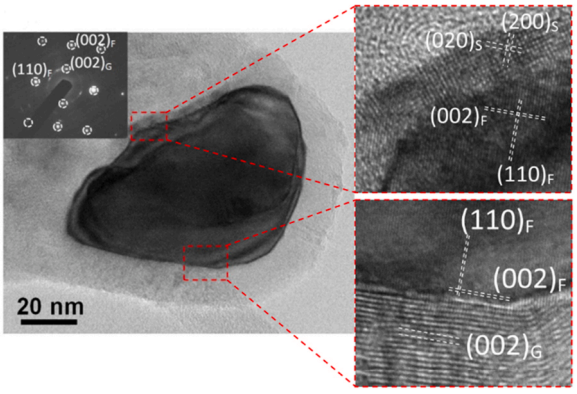

Fig. 4. TEM image of the Fe nanoparticle in the MN-C-600–6 with the corresponding SAED pattern. Upper inset is a HRTEM image of the Fe-iron oxide interface and the lower inset is the HRTEM of the Fe-graphite interface (S is cubic spinel iron oxide, F is BCC Fe and G is graphite).

epitaxially on the surface of the iron particle(s) at the parts where the graphitic shell is broken because of the partial oxidation of iron in contact with the ambient air. Sample MN-C-750–1 appears similar to sample MN-C-600–6; however, the contrast of the carbon matrix varies more (Fig. 3(b)). Samples MN-C-750–2 and MN-C-750–6 are composed of nanoparticles with two sizes: larger particles of approximately 40–50 nm in diameter and smaller particles of approximately 20 nm (Fig. 3(d) and (f)). The graphitic shell around the larger ones is mostly broken, while the smaller ones are predominately encapsulated (Fig. 3(d) and (f)). Empty graphitic shells are also clearly visible (Fig. 3(d) and (f)). The slight increase of the spinel iron oxide phase in the sample MN-C-750–6 relative to the MN-C-750–2 (Figs. 1 and 2) is most likely related to a larger number of the Fe nanoparticles being exposed to the air atmosphere in the sample MN-C-750–6 (more extensive braking of a graphitic shell). Those are more prone to the surface oxidation and thus more spinel iron oxide is formed.

To better characterize the carbon matrix, Raman spectroscopy was performed.

The first-order Raman spectrum of the MN-C (Fig. S3) shows only two broad poorly defined maxima centered at approx. 1300 cm^{-1} and 1600 cm^{-1}, indicating presence of graphitic and polyene structures. The first-order Raman spectra of the MN-C-T-t shows two broad peaks that are clearly composed of five individual bands (Fig. 5). The molecular approach to interpreting Raman spectra associates the G

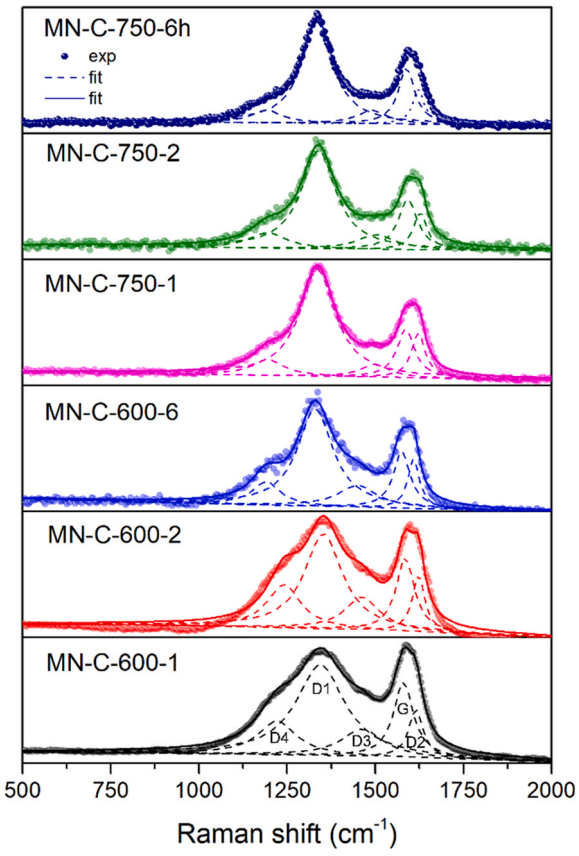

Fig. 5. Raman spectra of the carbonized samples. Dots represent experimental data, dashed lines individual bands fitted with a Lorentzian function and the full line is a sum of Lorentzian functions.

band with the stretching of all the pairs of sp^2 C atoms in rings and chains [28], D1 to breathing modes of the sp^2 C atoms in rings [28], D2 to the edges of the graphitic crystallites [29,30], D3 to the amorphous C phase [31,32] and D4 to the vibrations of polyenes [33]. The areas and the band positions of the G, D1 and D2 bands remained relatively constant during annealing (Fig. 5 and Table S1 in SI). However, the area of the D3 and D4 bands reduced significantly, indicating the disappearance of the amorphous C and the polyenes (Table T1 in SI). Usually, the ratio of I(D)/I(G) is used to estimate the crystal size of the graphite; however, in the presence of sp^3 C phases and when the expected size is significantly below 100 nm, the excitation-energy-independent G bands' half-width-at-half-maximum (HWHM) is used to estimate the lateral size of the graphite domain L_a, which is usually interpreted as the crystallite size of nanographite [28,34]. The estimated L_a remained practically constant during the annealing, between 6 and 7 nm (Table S1 in SI). An analysis of the spectra indicates that the nanocrystalline graphite, polyenes and amorphous carbon were formed within the first hour of annealing at 600 °C. The amount of graphite must be relatively low because it was not detected by the XRD analysis. During annealing at 600 °C the amounts of polyenes and amorphous carbon decrease, while only the number of graphitic domains increases. The process is much faster at 750 °C, where only after one hour of annealing, the intensities of the D3 and D4 bands (relative to the D1, D2, G bands) fall below those measured for any of the samples annealed at 600 °C. Furthermore, at 750 °C the D3 and D4 band intensities do not decrease significantly with an increasing annealing time.

To obtain a better insight into the formation of the graphite an EELS analysis in the STEM was performed for the two distinctly different samples: the MN-C-600–2 (XRD showed no graphite and

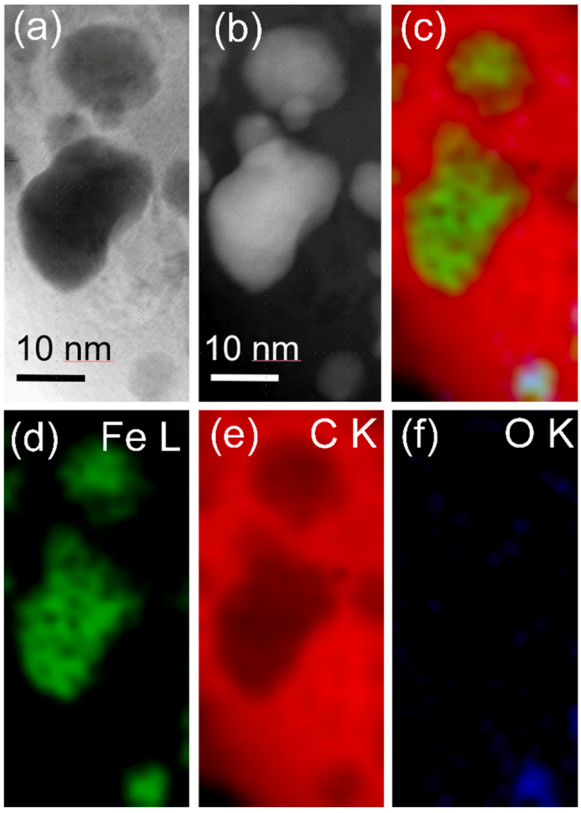

Fig. 6. BF (a) and HAADF (b) STEM images with corresponding elemental maps (d,e,f) showing distribution of Fe, C and O in the analyzed area of the MN-C-600–2 sample. Image (c) shows superimposition of the three elemental maps.

Fe_3C) and MN-C-750–2 (graphite and Fe_3C detected by XRD). Elemental mapping and analysis of the C K ELNES spectra enabled us to spatially differentiate between the iron oxide, Fe/Fe_3C, graphitic and non-graphitic carbon (Figs. 6 and 7).

Unfortunately, we could not differentiate between the Fe and Fe_3C nanoparticles because the differences in the Fe $L_{2,3}$ edge are below the resolution of our EELS system (~0.8 eV, FWHM of zero loss peak) and the C K edge is dominated by the C from the matrix. A detailed analysis of the C K ELNES enabled a visual representation of the spatial distribution of the graphitic and non-graphitic carbon in the form of maps (Figs. 8 and 9, see SI for details). We establish a ratio between the different regions of C K ELNES (A/B ratio) to distinguish between the two forms of carbon: for an A/B ratio > 1.2 the area is graphitic, for a ratio < 1.0 the area is non-graphitic and for the values in between the nature of the area cannot be interpreted [35,36].

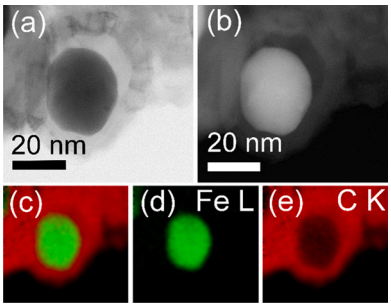

Fig. 7. BF (a) and HAADF (b) STEM images with corresponding elemental maps (d and e) showing distribution of Fe and C in the analyzed area of the MN-C-750–2 sample. Image (c) shows superimposition of the three elemental maps.

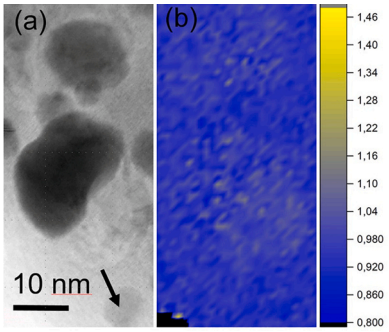

Fig. 8. BF STEM image (a) and A/B ratio map of the same area (b) of the MN-C-600–2. Yellow area is graphitic carbon and blue area non-graphitic. Iron oxide nanoparticle is marked with an arrow.

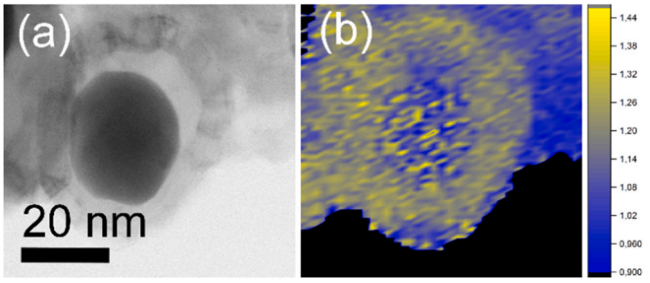

Fig. 9. BF STEM image (a) and A/B ratio map of the same area (b) of the MN-C-750–2. Yellow area is graphitic carbon and blue area non-graphitic.

The maps clearly show that the graphitic shells formed exclusively around the Fe/Fe_3C nanoparticles and not around the iron oxide nanoparticles.

The magnetic properties were measured at room temperature. The magnetizations are reported as magnetic moment per mass of sample *M* (Am^2/kg) in Fig. 10 (a) and as magnetic moment per mass of Fe that the nanocomposites contain *M* (Am^2/kg_{Fe}) in Fig. 10 (b). Magnetization as moment per mass of the sample reflects the total composition, considering non-magnetic phases as well. The magnetic nanoparticles MN show the highest saturation magnetization (moment per mass of the sample) of 62 Am^2/kg and practically zero coercivity and remanence, indicating their superparamagnetic nature (Fig. 10 (a) and S5 and Table 1). The saturation magnetization of the MN-C is significantly lower because of the incorporation of the magnetic nanoparticles in a non-magnetic matrix. The saturation magnetization of the MN-C-600–1 and MN-C-600–2 increased slightly, and the samples became ferri/ferromagnetic, displaying low values of coercivity and remanence, characteristic of magnetically soft Fe (Fig. 10 and S5 and Table 1).

As the time/temperature of the annealing increased the magnetization increased, reaching the highest value of 39.7 Am^2/kg in the sample MN-C-750–6 (Fig. 10 (a) and Table 1). The increase in the magnetization is not only related to the formation of Fe and Fe_3C, which both display higher saturation magnetizations of 217 Am^2/kg and 130 Am^2/kg, respectively [37], than the iron oxide, but also to the evaporation/decomposition of the non-magnetic carbon matrix during the annealing. The coercivity increased from 3.8 mT for the sample MN-C-600–1, reaching a maximum of 41 mT for the sample MN-C-600–6 and decreased to 21.5 mT for the sample MN-C-750–6 (Table 1 and Fig. S2). Among the three magnetic phases present in the samples, Fe_3C is magnetically the hardest and dominates the coercivity [37,38]. In general, the coercivity of the magnetic particles is a function of the crystallite size and has a maximum value just before the transition from the single domain to the multi-domain state [37]. The estimated crystallite size of the Fe_3C for the transition

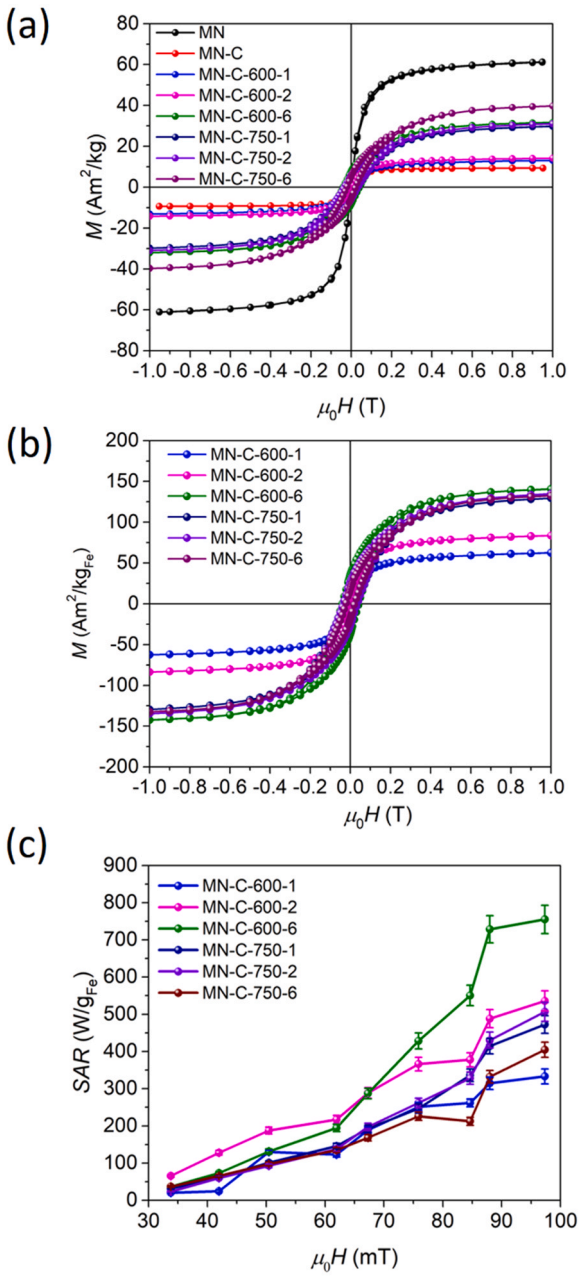

Fig. 10. Room-temperature magnetization curves normalized per mass of the sample (a), normalized per mass of the Fe (b) and *SAR* values normalized per mass of Fe (c).

is in the range 30–50 nm and for the spinel iron oxide and Fe it is well above 100 nm [37,38]. Most likely the MN-C-600–6 displays the highest coercivity because it contains Fe_3C particles in the single-domain regime, while all the MN-C-750-t samples contain larger, multi-domain nanoparticles. Because Fe is the only magnetic element present in all the magnetic phases, the saturation magnetization normalized per amount of Fe reflects the composition of the magnetic phases present in the sample. Sample MN-C-600–6 shows the highest saturation magnetization per kg of Fe (Fig. 10 (b)) because it contains, relatively speaking, the largest amount of Fe nanoparticles. Samples MN-C-750-t contain Fe_3C nanoparticles, which reduce their magnetization per kg of Fe. Among the MN-C-750-t samples their saturation magnetization directly reflects their varying ratios between the magnetic phases, i.e., samples MN-C-750–1 and MN-C-750–2 contain practically identical amounts of iron oxide, Fe and Fe_3C nanoparticles and their saturation

magnetization is also practically identical (Figs. 2 and 10 (b)). The sample MN-C-750–6 contains a significantly larger amount of Fe nanoparticles. However, the content of iron oxide nanoparticles increased as well; therefore, its saturation magnetization is only marginally higher than that of the former two samples (Figs. 2 and 10 (b)). The saturation magnetizations of the MN-C-600–1 and MN-C-600–2 samples are significantly smaller, reflecting their high content of iron oxide nanoparticles (Figs. 2 and 10 (b)).

The heating powers (*SAR*) generated by the samples in the AC-magnetic fields were determined from the temperature increase of their suspensions in isopropanol at a frequency of 273 kHz. The *SAR* values are normalized per gram of Fe that the sample contains as a function of the AC-magnetic field's amplitude (Fig. 10 (c)). Samples MN-C-600–1 and MN-C-600–2 show a monotonous, nearly linear increase and a saturation of the *SAR* value above 85 mT (Fig. 10 (c)). Sample MN-C-600–6 shows an abrupt increase of the *SAR* value above 60 mT and a saturation above 85 mT (Fig. 10 (c)). Above 60 mT the MN-C-600–6 displays the highest SAR value among the samples (Fig. 10 (c)). In contrast, the samples MN-C-750-t display a monotonic linear increase of the *SAR* value up to maximum AC-field amplitude of 97 mT (Fig. 10(c)).

3.2. Discussion

During carbonization of the precursor MN-C, three important transformations occur: the formation of graphite, the reduction of iron oxide to Fe and the formation of Fe_3C (Figs. 1 and 2). The formation of Fe/Fe_3C nanoparticles seems favorable from the application point of view, because the magnetization of the nanocomposites increases strongly (Table 1 and Fig. 10 (b)). However, measurements of the *SAR* clearly indicate the disadvantage of the Fe_3C, since composites containing the largest amounts of the Fe_3C exhibited the lowest *SAR* values (Fig. 10 (c)). In general, the *SAR* is proportional to the area of the dynamic hysteresis loop of the magnetic material [39].

Magnetically soft materials such as iron oxide, and especially Fe, that have a high magnetization are desirable because their dynamic hysteresis has a larger area at low AC-field amplitudes when compared to magnetically harder materials such as Fe_3C [40,41]. The MN-C-600–6 sample contains the largest amount of well-dispersed Fe nanoparticles in a graphitic matrix, giving it the best properties for the magnetic (induction) heating among the prepared samples. Moreover, the MN-C-600–6 sample exhibits a *SAR* value of approximately 800 W/g_{Fe}, a value that is, to the best of our knowledge, the highest for a high-surface-area magnetic-nanoparticles/carbon nanocomposite material [42]. The TEM, STEM and Raman analyses indicated that the small amount of graphite formed as soon as the Fe/Fe_3C nanoparticles formed at 600 °C. J. Hoekstra et al. [26] conducted a similar study and concluded that T > 715 °C is necessary for the carbothermal reduction of iron oxide to Fe, a temperature at which the Fe nanoparticles are already too mobile to become encapsulated by a graphitic shell and fully graphitize the amorphous carbon precursor by migration through the matrix, the so-called catalytic graphitization. In contrast, our results clearly show that the carbothermal reduction of iron oxide to Fe already proceeds at 600 °C; however, its kinetics is sluggish. More detailed TEM analyses revealed that a graphitic shell was also formed around the Fe nanoparticles (Fig. 3), protecting them well from ambient oxidation (Fig. S6 and table T2). As the temperature increased, the Fe/Fe_3C nanoparticles grew and migrated through the carbon matrix, leaving behind empty graphitic shells. During the process some of the larger Fe/Fe_3C nanoparticles burst the graphitic shell around them and became exposed to the atmosphere (Fig. 3(d) and (f) and Scheme 1). Upon exposure to the air a thin epitaxial layer of spinel iron oxide forms on the exposed surfaces of the Fe nanoparticles (Fig. 4). This thin oxide layer and a graphitic shell protect the Fe nanoparticles well from further oxidation, as is evident from the only marginal decrease of the magnetization of the nanocomposites, measured after being exposed to the air for one year (Fig. S6 and Table T2). The relative surface area of the nanocomposites decreased during the annealing because part of the carbon matrix decomposed/evaporated and because of the formation of Fe/Fe_3C, both of which have a higher density than the iron oxide (Fig. 2 and Table 1).

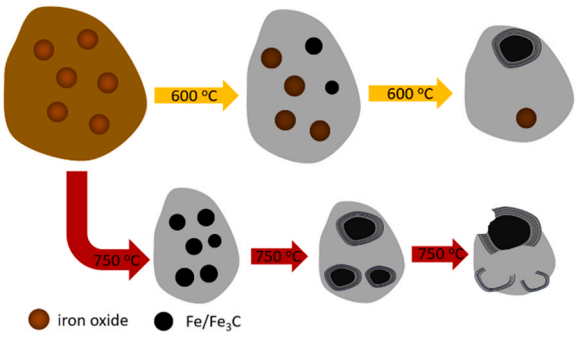

Scheme 1. Schematic representation of the magnetic-nanoparticles/carbon nanocomposite formation.

4. Conclusions

In conclusion, we prepared a series of magnetic carbon nanocomposites suitable for novel applications in magnetically heated catalysis. The nanocomposites were prepared by annealing a carbohydrate-coated iron oxide nanoparticle precursor in an inert atmosphere. During annealing at 600 °C the carbothermal reduction of iron oxide nanoparticles is relatively slow and a significant quantity of Fe nanoparticles was formed after only 6 h of annealing, while only a minor amount of Fe_3C was formed. Fe and Fe_3C nanoparticles were well encapsulated by a thin shell of polycrystalline turbostratic graphite, protecting them from aerial oxidation. Because of the high initial susceptibility and the large magnetization due to the Fe nanoparticles the nanocomposite annealed at 600 °C for 6 h exhibited an exceptionally high *SAR* value of approximately 800 W/g_{Fe}. The value is, to the best of our knowledge, the highest value for a high-surface-area magnetic carbon nanocomposite that exhibits excellent stability against oxidation. Increasing the annealing temperature to 750 °C accelerates the formation of Fe and Fe_3C nanoparticles. Their migration, promoted at the higher temperature, catalyzed the graphitization of the carbonaceous matrix, while their growth causes cracking of the graphitic shell and partially exposes their surface. An epitaxial layer of cubic spinel iron oxide is formed on those surfaces, providing their long-term stability against oxidation (in addition to the graphitic shell). Those nanocomposites containing larger amounts of magnetically hard Fe_3C had lower values of *SAR* that monotonically increased with the increasing field amplitude. The study clearly highlights the structure-properties relationship between iron-based nanoparticles in a carbon matrix and their properties with respect to magnetic heating and oxidation resistance. It also shows how the phase composition and nanostructuring can be controlled by the synthesis parameters, thereby providing an important basis for the optimization of nanocomposites for catalytic applications.

CRediT authorship contribution statement

Sašo Gyergyek: Conceptualization, Investigation, Writing – original draft, Writing – review & editing, Supervision. **Elena Chernyshova**: Formal analysis, Writing – review & editing. **Katalin Böőr**: Investigation, Writing – review & editing. **Marijan Nečemer**: Investigation, Formal analysis, Writing – review & editing. **Darko**

Makovec: Conceptualization, Investigation, Writing – review & editing, Funding acquisition.

Data availability

Data will be made available on request.

Declaration of Competing Interest

The authors declare that they have no known competing financial interests or personal relationships that could have appeared to influence the work reported in this paper.

Acknowledgments

The authors acknowledge the financial support from the Slovenian Research Agency (research core funding No. P2-0089). We acknowledge the CENN Nanocenter for the use of the Transmission Electron Microscope Jeol JEM-2100, Vibrating-Sample Magnetometer LakeShore 7400 Series VSM and Raman spectrometer NT-MDT model Integra Spectra for Materials Science. The author would like to thank Prof Andraž Kocjan from the JSI for the surface-area measurements and Dr Peter Kump for kindly providing the QAES (Quantitative Analysis of Environmental Samples) software (XRF).

Appendix A. Supporting information

Supplementary data associated with this article can be found in the online version at doi:10.1016/j.jallcom.2023.170139.

References

[1] Z.W. She, J. Kibsgaard, C.F. Dickens, I. Chorkendorff, J.K. Nørskov, T.F. Jaramillo, Combining theory and experiment in electrocatalysis: insights into materials design, Science 355 (2017) eaad4998, https://doi.org/10.1126/science.aad4998
[2] J. Hartwig, S. Ceylan, L. Kupracz, L. Coutable, A. Kirschning, Heating under high-frequency inductive conditions: application to the continuous synthesis of the neurolepticum olanzapine (Zyprexa), Angew. Chem. Int. Ed. 52 (2013) 9813–9817, https://doi.org/10.1002/anie.201302239
[3] S. Ceylan, C. Friese, C. Lammel, K. Mazac, A. Kirschning, Inductive heating for organic synthesis by using functionalized magnetic nanoparticles inside microreactors, Angew. Chem. Int. Ed. 47 (2008) 8950–8953, https://doi.org/10.1002/anie.200801474
[4] S.R. Chaudhuri, J. Hartwig, L. Kupracz, T. Kodanek, J. Wegner, A. Kirschning, Oxidations of allylic and benzylic alcohols under inductively-heated flow conditions with gold-doped superparamagnetic nanostructured particles as catalyst and oxygen as oxidant, Adv. Synth. Catal. 356 (2014) 3530–3538, https://doi.org/10.1002/adsc.201400261
[5] A. Meffre, B. Mehdaoui, V. Connord, J. Carrey, P.F. Fazzini, S. Lachaize, M. Respaud, B. Chaudret, Complex nano-objects displaying both magnetic and catalytic properties: a proof of concept for magnetically induced heterogeneous catalysis, Nano Lett. 15 (2015) 3241–3248, https://doi.org/10.1021/acs.nanolett.5b00446
[6] C. Niether, S. Faure, A. Bordet, J. Deseure, M. Chatenet, J. Carrey, B. Chaudret, A. Rouet, Improved water electrolysis using magnetic heating of FeC-Ni core-shell nanoparticles, Nat. Energy 3 (2018) 476–483, https://doi.org/10.1038/s41560-018-0132-1
[7] W. Wang, G. Tuci, C. Duong-Viet, Y. Liu, A. Rossin, L. Luconi, J.-M. Nhut, L. Nguyen-Dinh, C. Pham-Huu, G. Giambastiani, Induction heating: an enabling technology for the heat management in catalytic processes, ACS Catal. 9 (2019) 7921–7935, https://doi.org/10.1021/acscatal.9b02471
[8] A. Bordet, L.M. Lacroix, P.F. Fazzini, J. Carrey, K. Soulantica, B. Chaudret, Magnetically induced continuous CO2hydrogenation using composite iron carbide nanoparticles of exceptionally high heating power, Angew. Chem. Int. Ed. 55 (2016) 15894–15898, https://doi.org/10.1002/anie.201609477
[9] S. Gyergyek, A. Kocjan, M. Grilc, B. Likozar, B. Hočevar, D. Makovec, A hierarchical Ru-bearing alumina/magnetic iron-oxide composite for the magnetically heated hydrogenation of furfural, Green Chem. 22 (2020), https://doi.org/10.1039/d0gc00966k
[10] S. Gyergyek, A. Kocjan, A. Bjelić, M. Grilc, B. Likozar, D. Makovec, Magnetically separable Ru-based nano-catalyst for the hydrogenation/hydro-deoxygenation of lignin-derived platform chemicals, Mater. Res. Lett. 6 (2018) 426–431, https://doi.org/10.1080/21663831.2018.1477847
[11] A. Bjelić, M. Grilc, S. Gyergyek, A. Kocjan, D. Makovec, B. Likozar, Catalytic hydrogenation, hydrodeoxygenation, and hydrocracking processes of a lignin monomer model compound eugenol over magnetic Ru/C–Fe2O3 and mechanistic reaction microkinetics, Catalysts 8 (2018), https://doi.org/10.3390/catal8100425
[12] S. Gyergyek, D. Lisjak, M. Bekovič, M. Grilc, B. Likozar, M. Nečemer, D. Makovec, Magnetic heating of nanoparticles applied in the synthesis of a magnetically recyclable hydrogenation nanocatalyst, Nanomaterials 10 (2020) 1–9, https://doi.org/10.3390/nano10061142
[13] S. Gyergyek, M. Grilc, B. Likozar, D. Makovec, Electro-hydrogenation of biomass-derived levulinic acid to γ-valerolactone via the magnetic heating of a Ru nanocatalyst, Green Chem. 24 (2022) 2788–2794, https://doi.org/10.1039/D2GC00102K
[14] M. Besson, P. Gallezot, C. Pinel, Conversion of biomass into chemicals over metal catalysts, Chem. Rev. 114 (2014) 1827–1870, https://doi.org/10.1021/cr4002269
[15] H. Zhu, D. Yang, L. Zhu, H. Yang, D. Jin, K. Yao, A facile two-step hydrothermal route for the synthesis of gamma-Fe2O3 nanocrystals and their magnetic properties, J. Mater. Sci. 42 (2007) 9205–9209, https://doi.org/10.1007/s10853-007-1887-0
[16] Y. Yang, K. Chiang, N. Burke, Porous carbon-supported catalysts for energy and environmental applications: a short review, Catal. Today 178 (2011) 197–205, https://doi.org/10.1016/j.cattod.2011.08.028
[17] J. Kim, G.T. Neumann, N.D. McNamara, J.C. Hicks, Exceptional control of carbon-supported transition metal nanoparticles using metal-organic frameworks, J. Mater. Chem. A 2 (2014) 14014–14027, https://doi.org/10.1039/C4TA03050H
[18] Z. Gao, Y. Zhang, N. Song, X. Li, Biomass-derived renewable carbon materials for electrochemical energy storage, Mater. Res. Lett. 5 (2017) 69–88, https://doi.org/10.1080/21663831.2016.1250834
[19] J. Prasek, J. Drbohlavova, J. Chomoucka, J. Hubalek, O. Jasek, V. Adam, R. Kizek, Methods for carbon nanotubes synthesis - review, J. Mater. Chem. 21 (2011) 15872–15884, https://doi.org/10.1039/c1jm12254a
[20] X. Huang, R. Farra, R. Schlögl, M.-G. Willinger, Growth and termination dynamics of multiwalled carbon nanotubes at near ambient pressure: an in situ transmission electron microscopy study, Nano Lett. 19 (2019) 5380–5387, https://doi.org/10.1021/acs.nanolett.9b01888
[21] Y. Li, J. Liu, Y. Wang, Zhong Lin Wang, Preparation of monodispersed Fe-Mo nanoparticles as the catalyst for CVD synthesis of carbon nanotubes, Chem. Mater. 13 (2001) 1008–1014, https://doi.org/10.1021/cm000787s
[22] M.B. Martin, B. Dlubak, R.S. Weatherup, M. Piquemal-Banci, H. Yang, R. Blume, R. Schloegl, S. Collin, F. Petroff, S. Hofmann, J. Robertson, A. Anane, A. Fert, P. Seneor, Protecting nickel with graphene spin-filtering membranes: a single layer is enough, Appl. Phys. Lett. 107 (2015), https://doi.org/10.1063/1.4923401
[23] S. Gyergyek, D. Makovec, M. Jagodič, M. Drofenik, K. Schenk, O. Jordan, J. Kovač, G. Dražič, H. Hofmann, Hydrothermal growth of iron oxide NPs with a uniform size distribution for magnetically induced hyperthermia - structural, colloidal and magnetic properties, J. Alloy. Compd. 694 (2016), https://doi.org/10.1016/j.jallcom.2016.09.238
[24] M. Nečemer, P. Kump, J. Ščančar, R. Jaćimović, J. Simčič, P. Pelicon, M. Budnar, Z. Jeran, P. Pongrac, M. Regvar, K. Vogel-Mikuš, Application of X-ray fluorescence analytical techniques in phytoremediation and plant biology studies, Spectrochim. Acta Part B At. Spectrosc. 63 (2008) 1240–1247, https://doi.org/10.1016/j.sab.2008.07.006
[25] M. Nečemer, P. Kump, K. Vogel-Mikuš, Use of X-Ray fluorescence-based analytical techniques in phytoremediation, in: G. A. (Ed.), Handbook of Phytoremediation, New York, 2011, pp. 331–358.
[26] J. Hoekstra, A.M. Beale, F. Soulimani, M. Versluijs-Helder, J.W. Geus, L.W. Jenneskens, Base metal catalyzed graphitization of cellulose: a combined Raman spectroscopy, temperature-dependent X-ray diffraction and high-resolution transmission electron microscopy study, J. Phys. Chem. C 119 (2015) 10653–10661, https://doi.org/10.1021/acs.jpcc.5b00477
[27] L.M. Malard, M.A. Pimenta, G. Dresselhaus, M.S. Dresselhaus, Raman spectroscopy in graphene, Phys. Rep. 473 (2009) 51–87, https://doi.org/10.1016/j.physrep.2009.02.003
[28] A.C. Ferrari, J. Robertson, Raman spectroscopy of amorphous, nanostructured, diamond-like carbon, and nanodiamond, Philos. Trans. Ser. A Math. Phys. Eng. Sci. 362 (2004) 2477–2512, https://doi.org/10.1098/rsta.2004.1452
[29] M.A. Pimenta, G. Dresselhaus, M.S. Dresselhaus, L.G. Cançado, A. Jorio, R. Saito, Studying disorder in graphite-based systems by Raman spectroscopy, Phys. Chem. Chem. Phys. 9 (2007) 1276–1291, https://doi.org/10.1039/b613962k
[30] L.G. Cançado, M.A. Pimenta, B.R.A. Neves, M.S.S. Dantas, A. Jorio, Influence of the atomic structure on the Raman spectra of graphite edges, Phys. Rev. Lett. 93 (2004) 5–8, https://doi.org/10.1103/PhysRevLett.93.247401
[31] A. Cuesta, P. Dhamelincourt, J. Laureyns, A. Martínez-Alonso, J.M.D. Tascón, Raman microprobe studies on carbon materials, Carbon 32 (1994) 1523–1532, https://doi.org/10.1016/0008-6223(94)90148-1
[32] T. Jawhari, A. Roid, J. Casado, Raman spectroscopic characterization of some commercially available carbon black materials, Carbon 33 (1995) 1561–1565, https://doi.org/10.1016/0008-6223(95)00117-V
[33] B. Dippel, H. Jander, J. Heintzenberg, NIR FT Raman spectroscopic study of flame soot, Phys. Chem. Chem. Phys. 1 (1999) 4707–4712, https://doi.org/10.1039/a904529e
[34] P. Mallet-Ladeira, P. Puech, C. Toulouse, M. Cazayous, N. Ratel-Ramond, P. Weisbecker, G.L. Vignoles, M. Monthioux, Raman study to obtain crystallite size of carbon materials: a better alternative to the Tuinstra-Koenig law, Carbon 80 (2014) 629–639, https://doi.org/10.1016/j.carbon.2014.09.006
[35] V.J. Keast, A.J. Scott, R. Brydson, D.B. Williams, J. Bruley, Electron energy-loss near-edge structure - a tool for the investigation of electronic structure on the nanometre scale, J. Microsc. 203 (2001) 135–175, https://doi.org/10.1046/j.1365-2818.2001.00898.x

[36] J.W. Moreau, T.G. Sharp, A transmission electron microscopy study of silica and kerogen biosignatures in ~1.9 Ga Gunflint microfossils, Astrobiology 4 (2004) 196–210, https://doi.org/10.1089/153110704323175142
[37] J.M.D. Coey, Magnetism and Magnetic Materials, Cambridge Unversity Press, New York, 2010.
[38] S. Yamamoto, T. Terai, T. Fukuda, K. Sato, T. Kakeshita, S. Horii, M. Ito, M. Yonemura, Magnetocrystalline anisotropy of cementite pseudo single crystal fabricated under a rotating magnetic field, J. Magn. Magn. Mater. 451 (2018) 1–4, https://doi.org/10.1016/j.jmmm.2017.10.114
[39] R.E.E. Rosensweig, Heating magnetic fluid with alternating magnetic field, J. Magn. Magn. Mater. 252 (2002) 370–374, https://doi.org/10.1016/S0304-8853(02)00706-0
[40] J. Carrey, B. Mehdaoui, M. Respaud, Simple models for dynamic hysteresis loop calculations of magnetic single-domain nanoparticles: application to magnetic hyperthermia optimization, J. Appl. Phys. 109 (2011), https://doi.org/10.1063/1.3551582
[41] I.S. Poperechny, Y.L. Raikher, V.I. Stepanov, Dynamic magnetic hysteresis in single-domain particles with uniaxial anisotropy, Phys. Rev. B Condens. Matter Mater. Phys. 82 (2010) 1–14, https://doi.org/10.1103/PhysRevB.82.174423
[42] H. Gavilán, S.K. Avugadda, T. Fernández-Cabada, N. Soni, M. Cassani, B.T. Mai, R. Chantrell, T. Pellegrino, Magnetic nanoparticles and clusters for magnetic hyperthermia: optimizing their heat performance and developing combinatorial therapies to tackle cancer, Chem. Soc. Rev. 50 (2021) 11614–11667, https://doi.org/10.1039/D1CS00427A